



Simulating transient heat transfer in graphene at finite Knudsen number via the Boltzmann transport equation and molecular dynamics

Joel G. Christenson,^{1,2} Matthew P. Kroonblawd^{1,2},, Ryan A. Austin,² Laurence E. Fried,² and Ronald J. Phillips¹

¹*Department of Chemical Engineering, University of California-Davis, Davis, California 95616 USA*

²*Lawrence Livermore National Laboratory, 7000 East Ave., Livermore, California 94550 USA*



(Received 14 January 2020; revised 2 October 2020; accepted 6 October 2020; published 5 November 2020)

The phonon Boltzmann transport equation (BTE) with the relaxation time approximation (RTA) scattering model is used to calculate transient temperature profiles in graphene, and the results are compared to analogous molecular dynamics (MD) simulations. For the BTE calculations, the phonon dispersion relation and frequency-dependent scattering rates are obtained from a combination of MD data and semi-empirical power-law expressions for the normal and Umklapp phonon lifetimes. The dimensions and initial temperature conditions of graphene are varied to study the size and temperature dependence of thermal transport physics at the mesoscopic scale. Good quantitative agreement to within 5% is found between the BTE and MD results, over a wide range of temperatures and lengthscales of the temperature variation in the graphene sheet. Small differences are attributed to the inaccuracy of the RTA as applied to graphene, and to neglecting four-phonon scattering in the BTE simulations. The present results may further understanding in applications such as the transient heating of nanoelectronics.

DOI: [10.1103/PhysRevB.102.205406](https://doi.org/10.1103/PhysRevB.102.205406)

I. INTRODUCTION

Heat transfer at the nanoscale is an active area of research with applications in diverse fields such as microelectronic devices, thermoelectric materials, and high-energy-density materials used to make explosives [1–7]. For such problems, lengthscales and timescales can be comparable to the phonon mean free path and relaxation time, respectively. Under these conditions, energy transfer by phonons is at least partially ballistic rather than fully diffusive, and the application of the continuum heat equation with Fourier's conduction law leads to overestimated heat fluxes. Therefore, alternative methods are needed to address these problems.

In this work, we assess the use of the phonon Boltzmann transport equation (BTE) to calculate time-dependent thermal phenomena in graphene, at lengthscales where there is a significant ballistic heat flux contribution. Graphene is a two-dimensional lattice of carbon atoms with one of the highest known in-plane thermal conductivities [8], making it an attractive material for microelectronic cooling applications [9]. The BTE describes the evolution of the phonon distribution function via a quasiparticle description, which is valid when phonon wavelengths are much smaller than the characteristic lengthscales of interest. The BTE has been successfully applied to graphene in numerous studies that fall into two classes [2,10]. The first treats the collision dynamics of the BTE in a more complete sense, often under the assumption that three-phonon processes are the dominant scattering mechanisms [2,11–15]. A second class of solutions incorporates the relaxation time approximation (RTA), which linearizes the collisional dependence of the BTE, and which is the focus of this study.

Methods in the first class offer great predictive power. For example, Fugallo *et al.* [14] and Lindsay *et al.* [15] calculated temperature-dependent thermal conductivities in graphite and graphene, and obtained excellent agreement with experimental data. However, the more complete treatment of collision dynamics is computationally expensive, possibly precluding its use for studying transient energy transfer [2,10].

The RTA employed by the second class greatly simplifies the solution of the BTE, relative to the first approach, by linearizing its collisional dependence. To assess the accuracy of the RTA, Ward and Broido [16] calculated temperature-dependent thermal conductivities in Si and Ge, and showed that, compared to a more sophisticated approach which includes the full collision dependence of the BTE (with three-phonon interactions), the RTA introduces a 5–10% error over the temperature range 100–800 K. The RTA has been found to be less accurate in materials such as graphene, which have a strong normal, momentum-conserving scattering contribution at room temperature [10,13–15,17]. For example, Lindsay *et al.* [15] found that the RTA underestimates thermal conductivities in graphene if relaxation times are taken to be the inverse of scattering rates. The authors note that this underprediction is due to the RTA overemphasizing the effects of Umklapp phonon collisions, which return the system to the Bose-Einstein distribution and act as an impedance to the heat flux [15,18]. Despite its shortcomings, Aksamija and Knezevic [19–21] still found the RTA to be useful for graphene.

In this study, we further examine the applicability and limitations of the BTE, with the RTA, for describing nanoscale heat transfer in graphene. Our approach involves calculating thermal transients in graphene sheets using both the BTE, with the RTA, and molecular dynamics (MD) for comparison.

Existing transient BTE-based studies of graphene are scarce [17,22]. Most related studies tend to focus on the steady state, often using the accuracy of thermal conductivity calculations as a measure of performance. For transient calculations, ballistic transport, thermal conduction, and the heat capacity all contribute to the temperature dynamics. Therefore, it remains unclear whether steady-state calculations are a good gauge of the BTE's ability to describe thermal transients in graphene. Such information is desirable for modeling transient heating of nanoelectronics, wherein heat pulses can occur over 50–100 ps [23], which is on par with or shorter than typical phonon lifetimes in graphene and silicon [24–26]. We demonstrate that the simplified collisional dependence of the BTE yields excellent transient temperature predictions, relative to MD, under certain size and temperature constraints, elucidating the conditions under which both theories are valid.

II. BOLTZMANN TRANSPORT EQUATION

A. Governing equations

The phonon BTE is given by

$$\frac{\partial g_{\omega_l}}{\partial t} + \mathbf{v}_{g,\omega_l} \cdot \nabla g_{\omega_l} = \left. \frac{\partial g_{\omega_l}}{\partial t} \right|_{\text{coll}}, \quad (1)$$

where $g_{\omega_l}(\mathbf{r}, t, \Omega)$ is the phonon energy distribution function, $\Omega = (\theta, \varphi)$ is the direction of phonon travel, \mathbf{v}_{g,ω_l} is the phonon group velocity, and ω_l subscripts signify frequency dependence for phonon branch l . The right side of Eq. (1) represents the collision operator associated with phonon scattering. In this work, we make use of the RTA [2,18,27], linearizing that term as

$$\left. \frac{\partial g_{\omega_l}}{\partial t} \right|_{\text{coll}} = \frac{g_0 - g_{\omega_l}}{\tau_{\omega_l}}, \quad (2)$$

where g_0 denotes the equilibrium distribution function of the phonon energy, and τ_{ω_l} the branch-specific phonon relaxation time.

The RTA assumes that the out-of-equilibrium distribution g_{ω_l} tends towards the equilibrium distribution g_{0,ω_l} at a rate inversely proportional to τ_{ω_l} , implying that all phonon collisions are directly responsible for bringing the system to equilibrium. However, this is only true for Umklapp, or resistive phonon collisions. Consequently, when temperatures are low relative to the Debye temperature, the RTA has been found to underestimate the thermal conductivity in materials such as graphene for which normal collisions are the dominant scattering mechanism [10,13–15,17]. In such cases, the Callaway method, which distinguishes between normal and resistive scattering, has been shown to be a better predictor of thermal transport properties in graphene [10,13,17,22,28,29]. However, the Callaway approach requires explicit scattering rates for normal and resistive processes, which are not always available, and in particular, are not readily available for the optical branches of graphene. It is therefore of interest to see what insights can be gained with the simpler RTA approximation.

Noting that, under the RTA, Eq. (1) contains the unknown functions g_{ω_l} and g_0 , an additional constraint is needed. Integrating Eq. (1) over frequency and solid angle, summing

over all phonon branches, and enforcing macroscopic energy conservation, yields

$$\sum_{l=1}^{N_B} \int_{\partial\omega_l} \int_{\partial\Omega} \left(\frac{g_0 - g_{\omega_l}}{\tau_{\omega_l}} \right) d\omega_l d\Omega = 0, \quad (3)$$

where N_B is the total number of phonon branches ($N_B = 6$ for graphene). In addition, we expand the temperature dependence of g_0 around a reference temperature T_0 [30]. With a single, linear term, this leads to

$$g_0 = \frac{1}{4\pi} C_{\omega_l} \Big|_{T_0} (T - T_0), \quad (4)$$

where the spectral heat capacity C_{ω_l} is given by

$$C_{\omega_l} \Big|_{T_0} = \hbar\omega_l D_{\omega_l} \frac{\partial f_{\text{BE}}}{\partial T} \Big|_{T_0}. \quad (5)$$

Here, D_{ω_l} is the phonon density of states, and f_{BE} the Bose-Einstein distribution,

$$f_{\text{BE}} = \frac{1}{\exp\left(\frac{\hbar\omega_l}{k_B T}\right) - 1}, \quad (6)$$

where \hbar is the reduced Planck constant, and k_B is the Boltzmann constant. Effects of including a second, quadratic term in Eq. (4) are examined in Sec. IV C below.

B. Numerical implementation for graphene

The BTE is numerically difficult to solve due to its high dimensionality. A general time-dependent problem with three spatial dimensions has a total of seven degrees of freedom, per phonon branch, when frequency and angular dependence are included. The following discussion presents our numerical method of solution. For simplicity, we focus on cases with spatial variations in only one direction within a graphene sheet. The method can easily be extended to problems with variations in two spatial directions.

1. Problem discretization

We use the discrete ordinates method (DOM) to numerically evaluate the angular dependence of phonon travel. In general, the DOM is implemented by subdividing θ and φ into N_θ and N_φ parts, i.e., $\theta \rightarrow \{\theta_i, i = 1, 2, \dots, N_\theta\}$, and $\varphi \rightarrow \{\varphi_j, j = 1, 2, \dots, N_\varphi\}$, where $0 \leq \theta_i \leq \pi$ and $0 \leq \varphi_j \leq 2\pi$, for all i, j . Here we consider a graphene sheet aligned with the x - z plane, with temperature variations occurring only in the z direction, so that there is no φ or x -dependence [Fig. 1(b)]. The DOM then yields the family of distribution functions $g_{\omega_l,i} = g_{\omega_l,i}(t, z, \theta_i)$, whose evolution is described by Eq. (1). To approximate the solid angle integral in Eq. (3), the θ_i are chosen to coincide with the abscissae of the Legendre-Gauss quadrature rule

$$\int_0^\pi f(\theta) d\theta \simeq \frac{\pi}{2} \sum_{i=1}^{N_\theta} W_i f(\theta_i), \quad (7)$$

with $\theta_i = (\pi/2)\tilde{\theta}_i + \pi/2$, and where the weights, W_i , and abscissae, $\tilde{\theta}_i$, are tabulated for different values of N_θ [31].

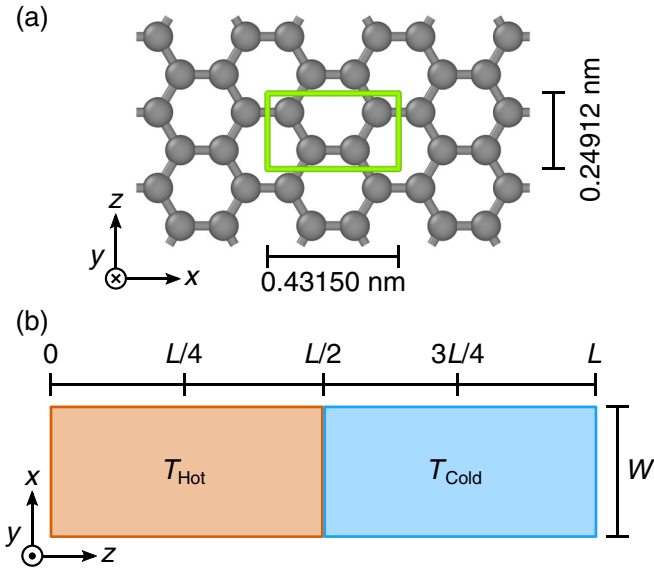


FIG. 1. (a) Snapshot showing a $3 \times 1 \times 3$ replication of the orthorhombic graphene primary cell with the periodic cell edges drawn with green lines rendered using OVITO [32]. (b) Initial value problem setup for simulations of transient energy transport.

The frequency integral in Eq. (3) is numerically calculated using the trapezoidal rule. For a particular branch l , the partition of ω_l takes the form $\{\omega_{l,m}, m = 1, 2, \dots, N_{\omega}\}$, where the end points $\omega_{l,1}$ and $\omega_{l,N_{\omega}}$ correspond to the minimum and maximum frequencies within that branch, respectively, and where the interior points are ordered, i.e., $\omega_{l,2} < \dots < \omega_{l,N_{\omega}-1}$. A general frequency integral is then approximated as

$$\int_{\partial\omega_l} f(\omega)d\omega \simeq \sum_{m=1}^{N_{\omega}-1} \frac{1}{2} [f(\omega_{m+1}) + f(\omega_m)](\omega_{m+1} - \omega_m). \quad (8)$$

The spatial and temporal derivatives in Eq. (1) are discretized using finite differences. The time derivative is approximated by the implicit Euler method, and the spatial derivative by a first-order upwind scheme

$$\begin{aligned} & \frac{g_{\omega_{(l,m)},i,k}^{n+1} - g_{\omega_{(l,m)},i,k}^n}{\Delta t} \\ & + \cos(\theta_i) v_{g,\omega_{(l,m)}} \frac{g_{\omega_{(l,m)},i,k+\alpha}^{n+1} - g_{\omega_{(l,m)},i,k+\alpha-1}^{n+1}}{\Delta z} \\ & = \frac{\frac{1}{\pi} C_{\omega_{(l,m)}} \Big|_{T_0} (T_k^{n+1} - T_0) - g_{\omega_{(l,m)},i,k}^{n+1}}{\tau_{\omega_{(l,m)},k}^{n+1}}, \end{aligned} \quad (9)$$

where $\alpha = 1$ for $\cos \theta_i < 0$, $\alpha = 0$ for $\cos \theta_i > 0$, n superscripts denote the temporal index, with time step Δt , and k subscripts the spatial index, with grid spacing Δz . In Eq. (9), the spectral heat capacity depends on neither time nor space due to its evaluation at the reference temperature T_0 , as a result of linearizing the temperature dependence of g_{0,ω_l} in Eq. (4). Additionally, in light of the frequency data discussed below, we assumed that the group velocities are also temporally and spatially independent, but have allowed for the relaxation times to vary with these quantities. Finally, we note that the

factor $(4\pi)^{-1}$ appearing in Eq. (4) is replaced by π^{-1} to account for the two-dimensionality of graphene.

Applying the integral approximations Eqs. (7) and (8) allows us to write the energy conservation constraint Eq. (3) as

$$\begin{aligned} & \frac{\pi}{2} \sum_{l=1}^{N_B} \sum_{m=1}^{N_{\omega}-1} \sum_{i=1}^{N_{\theta}} \frac{W_i}{2} \\ & \times \left[\frac{g_{\omega_{(l,m+1)},i,k}^{n+1} - \frac{1}{\pi} C_{\omega_{(l,m+1)}} \Big|_{T_0} (T_k^{n+1} - T_0)}{\tau_{\omega_{(l,m+1)},k}^{n+1}} \right. \\ & \left. + \frac{g_{\omega_{(l,m)},i,k}^{n+1} - \frac{1}{\pi} C_{\omega_{(l,m)}} \Big|_{T_0} (T_k^{n+1} - T_0)}{\tau_{\omega_{(l,m)},k}^{n+1}} \right] \\ & \times (\omega_{l,m+1} - \omega_{l,m}) = 0. \end{aligned} \quad (10)$$

Equations (9) and (10) are a discretized system of algebraic equations for the unknowns $g_{\omega_{(l,m)},i,k}^{n+1}$ and T_k^{n+1} , which can be solved iteratively, for example, by Newton's method [33]. We achieved convergence to 1×10^{-4} K by the simpler method of fixed-point iteration, typically within two to five iterations per time step.

2. Boundary and initial conditions

Boundary conditions are derived by specifying the properties of phonons entering the domain. For a one-dimensional problem with the endpoints $z = 0$ and $z = L$, boundary conditions at $z = 0$ describe rightward traveling phonons, for which $\cos \theta_i > 0$, and conditions at $z = L$ correspond to phonons traveling to the left with $\cos \theta_i < 0$. In the simulations to follow, we make use of periodic boundary conditions, and an initial temperature condition. Periodicity requires

$$g_{\omega_{(l,m)},i,0}^n = g_{\omega_{(l,m)},i,N_z}^n, \quad (11)$$

where $N_z \Delta z = L$ represents the right-hand boundary.

We specify an initial temperature condition at $t = 0$ ($n = 0$) as

$$g_{\omega_{(l,m)},i,k}^0 = \frac{1}{\pi} C_{\omega_{(l,m)}} \Big|_{T_0} (T_{\text{init},k} - T_0), \quad (12)$$

where T_{init} is the desired initial temperature distribution.

C. Frequency parameters

Several frequency-dependent parameters are needed to solve the BTE form described above, including τ_{ω_l} , v_{g,ω_l} , and C_{ω_l} . We note that previous BTE-based studies of graphene involved the calculation of the thermal conductivity at steady state, for which some, or all of the optical phonons are omitted due to their relatively small contribution [10,19]. However, since we are considering transient calculations, an analogy to the continuum heat equation suggests that both the conductivity and heat capacity play important roles in thermal transport. We therefore include the optical phonons due to their ability to store energy [18].

To obtain the frequency-dependent phonon group velocities, we adopt the phonon dispersion relation calculated at

300 K by Koukaras *et al.* [34]. Due to the relatively symmetric shape of the graphene dispersion relation, we assume that the first Brillouin zone is isotropic in the Γ - K direction. Other groups found success using an isotropic approximation in the Γ - M direction [10]. We calculate the branch-specific phonon group velocities by numerically differentiating a linear interpolation of each branch of the dispersion relation according to

$$v_{g,\omega_l} = \frac{\partial \omega_l}{\partial k}, \quad (13)$$

where k is the wave vector. The frequency dependence of the forthcoming equations is evaluated by setting the maximum and minimum frequencies within each branch along the Γ - K direction to $\omega_{l,\max}$ and $\omega_{l,\min}$, respectively, and discretizing the frequency range between the two endpoints as described previously.

From Eqs. (5) and (6), the spectral heat capacity C_{ω_l} is expressed as

$$C_{\omega_l} \Big|_{T_0} = \frac{(\hbar \omega_l)^2}{k_B T_0^2} D_{\omega_l} \frac{e^{\hbar \omega_l / k_B T_0}}{(e^{\hbar \omega_l / k_B T_0} - 1)^2}. \quad (14)$$

The bulk, or total volumetric heat capacity C is then given by

$$C = \sum_{l=1}^{N_B} \int_{\partial \omega_l} C_{\omega_l} \Big|_{T_0} d\omega_l, \quad (15)$$

for which the classical, or high-temperature limit is

$$C^\infty = \lim_{T_0 \rightarrow \infty} C = k_B \sum_{l=1}^{N_B} \int_{\partial \omega_l} D_{\omega_l} d\omega_l. \quad (16)$$

To calculate the heat capacity, we use the density of states for an isotropic two-dimensional (2D) material [18,35]

$$D_{\omega_l} = \frac{k}{2\pi v_{g,\omega_l}}. \quad (17)$$

We assess the error associated with using the simplified density of states Eq. (17) by comparing the high-temperature limit of the heat capacity predicted by Eq. (16) with the theoretical limit for graphene

$$C_{\text{th}}^\infty = 3nk_B, \quad (18)$$

where n is the atomic number density (per unit area) of graphene. Taking $n = 3.82 \times 10^{19}$ atoms/m² [8] yields $C_{\text{th}}^\infty = 1.58 \times 10^{-3}$ JK⁻¹m⁻², while Eq. (16) gives $C^\infty = 1.82 \times 10^{-3}$ JK⁻¹m⁻². We note that C in Eq. (15) equals C_{th}^∞ at 1190 K.

Our relaxation times τ_{ω_l} are obtained by using the approach of Ward and Broido [16], who calculated accurate thermal conductivities in silicon and germanium with the RTA, using a relaxation time of the form [16,36]

$$\frac{1}{\tau_{\omega_l}} = \frac{1}{\tau_N} + \frac{1}{\tau_U}. \quad (19)$$

Equation (19) is an application of the Matthiessen rule [18], where τ_N represents the relaxation times corresponding to the so-called normal, or momentum-conserving scattering processes, and τ_U represents the rates for resistive, or Umklapp scattering. The combined relaxation time Eq. (19) should

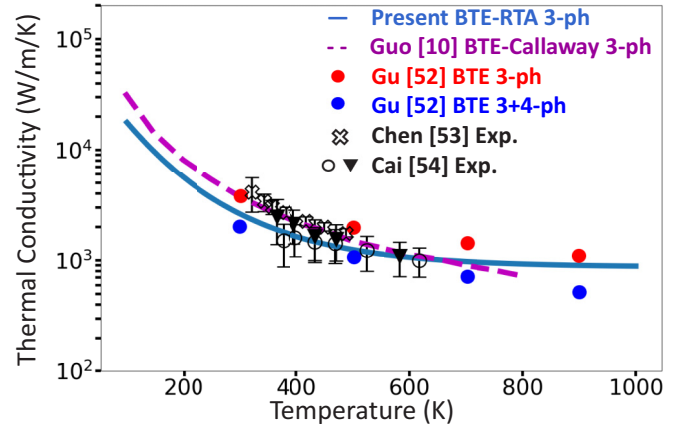


FIG. 2. Temperature-dependent bulk thermal conductivities, including data from Guo and Wang [10], Gu *et al.* [52], Chen *et al.* [53], and Cai *et al.* [54].

become more accurate as temperatures approach the Debye temperature, when in terms of calculating the conductivity, normal, and Umklapp processes are indistinguishable [36].

We use empirical power-law expressions for the three-phonon normal and Umklapp relaxation times, which were used in previous studies of graphene [10,19,37,38]. The three-phonon Umklapp lifetimes for the longitudinal acoustic and transverse acoustic (LA and TA) branches are given by [10,19,37–39]

$$\frac{1}{\tau_U(\omega_l, T)} = B_U \omega_l^2 T \exp(-\Theta_l / 3T), \quad (20)$$

where $B_U = \hbar \gamma_l^2 / (M \Theta_l v_{s,l}^2)$. In these expressions, γ_l represents the per-branch Grüneisen parameters which are taken to be 2 and 2/3 for the LA and TA branches, respectively [10], M represents the molecular mass of carbon, which is assumed to be purely carbon-12, $v_{s,l}$ represents the speed of sound in graphene, which is approximated as the group velocity near the Γ point and calculated to be 19.3 nm ps⁻¹ for the LA branch and 14.2 nm ps⁻¹ for TA. The parameter Θ_l is the branch-specific Debye temperature given by [37]

$$\Theta_l^2 = \frac{5\hbar^2}{3k_B^2} \frac{\int \omega_l^2 D_{\omega_l} d\omega_l}{\int D_{\omega_l} d\omega_l}, \quad (21)$$

which we calculate as 1814 and 1586 K for the LA and TA branches, respectively. The three-phonon normal lifetimes for the LA and TA branches are expressed as [10,38,39]

$$\frac{1}{\tau_N(\omega_l, T)} = B_N \omega_l T^3, \quad (22)$$

where $B_N = k_B^3 \gamma_l^2 V^{(2/3)} / (\hbar^2 M v_{s,l}^4)$, and V is the average volume per carbon atom in graphene, which is taken to be 8.769×10^{-30} m³ [10].

We note that Eqs. (20) and (22) have often been used for the acoustic LA, TA, and ZA (out-of-plane) branches of graphene. However, such expressions may only be accurate for the LA and TA branches because they are typically obtained under a linear dispersion assumption, whereas the frequency dependence of the ZA branch is quadratic near the Γ point [40–42]. We found Eqs. (20) and (22) to yield unphysically

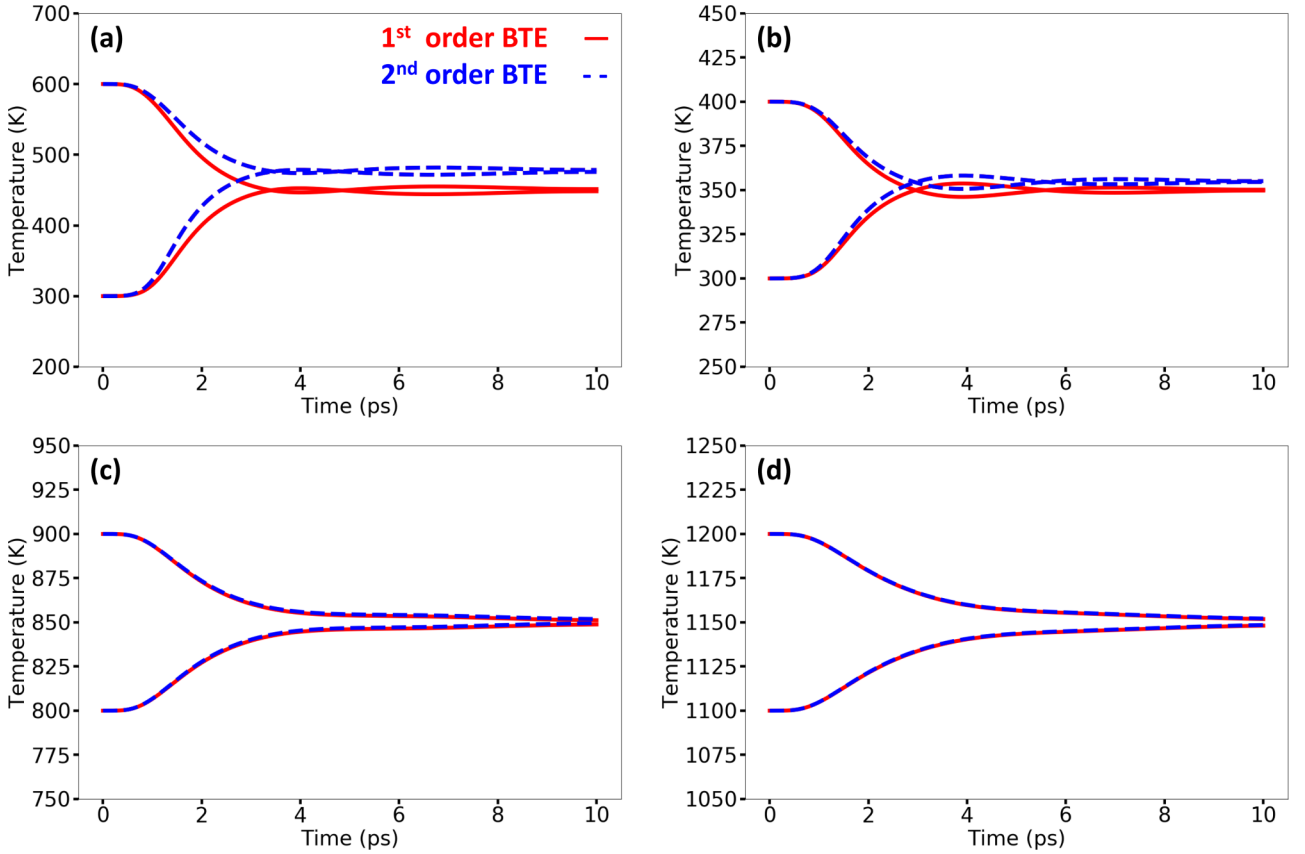


FIG. 3. Comparisons between first- and second-order temperature expansions of the Bose-Einstein distribution, $T(L/4, t)$ (top curves) and $T(3L/4, t)$ (bottom curves), for the $L = 50$ nm case. (a) $T_{\text{Hot}} = 600$ K, $T_{\text{Cold}} = 300$ K, (b) $T_{\text{Hot}} = 400$ K, $T_{\text{Cold}} = 300$ K, (c) $T_{\text{Hot}} = 900$ K, $T_{\text{Cold}} = 800$ K, and (d) $T_{\text{Hot}} = 1200$ K, $T_{\text{Cold}} = 1100$ K.

small relaxation times for the ZA branch. Therefore, we only apply these expressions to the LA and TA branches. The lifetimes for the remaining ZA and optical branches (LO, TO, ZO) are obtained from Zou *et al.* [24], who reported MD-calculated relaxation times for graphene along the Γ - K direction, as a function of frequency at 300 K. Due to the relatively flat dispersion of the optical branches, we assign a uniform frequency-independent value of τ_{ω_i} to each of the LO, TO, and ZO branches, which we take to be the mean relaxation time within each branch, respectively. Therefore, only the relaxation times for the LA and TA branches are functions of temperature. This approximation is satisfactory for the following BTE and MD comparisons because in MD simulations, the LA and TA branches account for 70% of the thermal conductivity in graphene, at room temperature [24].

III. MOLECULAR DYNAMICS

Classical molecular dynamics (MD) simulations of free-standing graphene sheets were performed using LAMMPS [43] and a version of the Tersoff force field [44,45] that was specifically parametrized by Lindsay and Broido [46] (hereafter, Tersoff-2010) to accurately capture the vibrational density of states for graphene and related materials. All MD-derived parameters for the BTE taken from the literature were obtained using the same Tersoff-2010 force field model. Simulation cells were treated as three-dimensional (3D) periodic,

with the graphene sheet extending through two of the three periodic boundaries and with a large 50-nm vacuum region added in the third dimension to prevent self interactions. Equilibrium simulations were performed to prepare initial configurations that sampled the isothermal-isochoric (NVT) and isothermal-isostress ($N\sigma T$) ensembles. Simulations of transient energy transport were performed in the isochoric-isoenergetic (NVE) ensemble. All trajectories were integrated with a 0.5-fs time step. Isothermal sampling was performed using a Nosé-Hoover-style thermostat [47,48] and isostress sampling was performed with a Nosé-Hoover-style barostat [49] in which the three independent in-plane stress components of the sheet were coupled to their respective cell lengths and cell angle.

All production simulation cells were constructed using a lattice constant of $a = 0.24912$ nm, which was obtained from a 100 ps $N\sigma T$ simulation of a nonorthorhombic 16×16 graphene supercell containing 512 atoms at 300 K and 1 atm. The generalized crystal-cutting method [50] (GCCM) was used to obtain an oriented orthorhombic primary cell for graphene, shown in Fig. 1(a), that contained four atoms and had (x, y, z) dimensions (0.43150, 50.000, 0.24912 nm). Supercells for probing one-dimensional (1D) transient energy transport along z were prepared by replicating the primary cell along x and z following the schematic shown in Fig. 1(b). We set the simulation cell width W transverse to the conduction direction to be 10.356 nm (24 replications) and considered

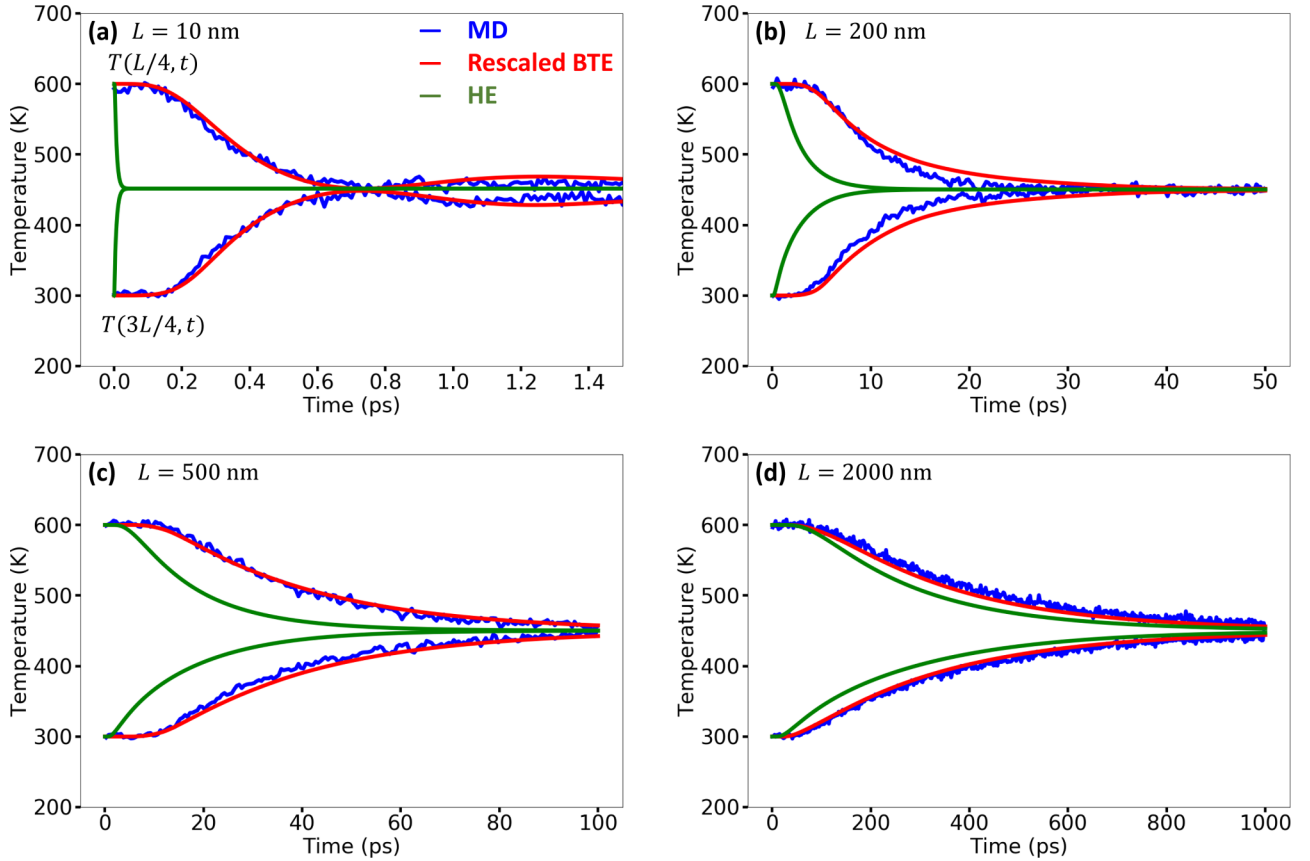


FIG. 4. (a) Transient temperatures $T(L/4, t)$ (top curves) and $T(3L/4, t)$ (bottom curves) with $T_0 = 450$ K for $L = 10$ nm, (b) $L = 200$ nm, (c) $L = 500$ nm, (d) $L = 2000$ nm. “Rescaled BTE” refers to the BTE with the classical heat capacity Eq. (16).

simulation cell lengths L along the conduction direction of between ≈ 10 to ≈ 2000 nm (40 to 8000 replications). The smallest supercell contained 3840 atoms and the largest contained 384 000.

Initial states for simulations of 1D transient energy transport were prepared through a multistep process. First, the entire supercell was equilibrated at temperature T_{Cold} through a 1-ns NVT simulation. A nonequilibrium step-wise temperature distribution was imposed by dividing the supercell in half equally along z to form hot and cold regions. While holding atoms in the cold region in fixed positions, we heated the atoms in the hot region to T_{Hot} through a 50-ps NVT simulation in which velocities were randomly re-selected from the Maxwell distribution at T_{Hot} every 1 ps for the first 5 ps. An analogous velocity randomization and equilibration procedure was then applied to the atoms in the cold region with temperature T_{Cold} while holding the atoms in the hot region fixed. Following from this state, we simulated the relaxation of the initial temperature distribution towards equilibrium through NVE trajectory integration. The temperature profile $T(z, t)$ was recorded every 10 fs during the relaxation simulation by binning the supercell into contiguous, nonoverlapping 0.99648 nm bins along z , yielding discrete samples that correspond to the instantaneous average kinetic temperature of the 384 atoms in each bin. Ensembles of ten independent relaxation simulations were performed for each supercell size, aside from the largest (≈ 2000 nm) for which we ran five independent simulations. All MD predictions for $T(z, t)$ re-

ported below correspond to ensemble averages. Additional smoothing was performed by block-averaging in time within contiguous nonoverlapping windows. Window sizes ranged between 0.05 and 2 ps, with larger windows used for larger (and thus longer) simulations. We verified that our results were independent of W for cases with $L \leq 50$ nm by performing an analogous set of simulations with $W = 51.780$ nm (120 replications along x).

IV. RESULTS AND DISCUSSION

We assess the accuracy of our BTE formulation by first calculating values for the thermal conductivity, and comparing to results from the literature. We then use our numerical solver to compute thermal transients in graphene for a range of conditions, and compare to analogous results obtained by MD and from the continuum heat equation (HE). As discussed in the Supplemental Material [51], our solver was verified by demonstrating convergence between the BTE and HE for problem sizes approaching the continuum scale, i.e., for problems with small Knudsen number Kn , where Kn is the ratio of the phonon mean free path to the problem’s characteristic lengthscale.

For simulations of transient temperature changes, we use the periodic graphene sheet with an initial step change in temperature shown in Fig. 1(b). The lengthscale L is the distance over which the temperature variation is repeated in the z -direction. The initial temperature is set such that $T(z, 0) =$

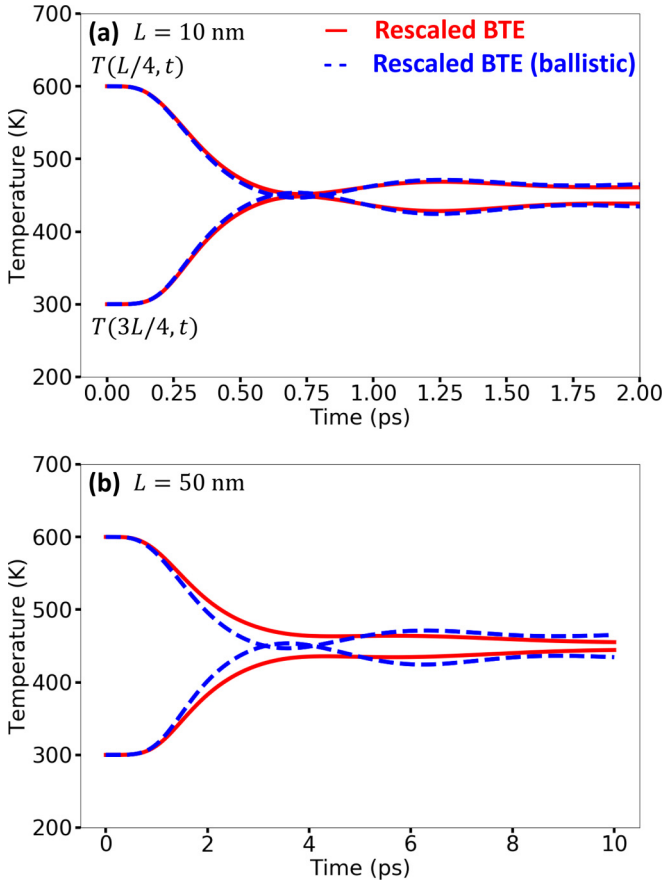


FIG. 5. Transient temperatures $T(L/4, t)$ (top curves) and $T(3L/4, t)$ (bottom curves) for (a) $L = 10$ nm and (b) 50 nm.

T_{Hot} for $0 \leq z < L/2$, $T(z, 0) = T_{\text{Cold}}$ for $L/2 < z \leq L$, and $T(L/2, 0) = (T_{\text{Hot}} + T_{\text{Cold}})/2$, where T_{Hot} and T_{Cold} are varied. Additionally, periodic boundary conditions are prescribed at $z = 0$ and $z = L$, and the reference temperature T_0 is set to $(T_{\text{Hot}} + T_{\text{Cold}})/2$. There is no temperature variation in the x -direction, which plays no role in the BTE simulations.

A. Temperature-dependent thermal conductivity predictions

To assess the validity of the frequency-dependent parameters presented in Sec. II C, we calculated the RTA thermal conductivity given by

$$\kappa = \frac{1}{2} \sum_{l=1}^{N_B} \int_{\omega_l} \tau_{\omega_l} v_{g,\omega_l}^2 C_{\omega_l} \Big|_{T_0} d\omega_l, \quad (23)$$

and compare to various literature sources in Fig. 2. The experimental results of Chen *et al.* [53] (isotopically purified 0.01% ^{13}C) and Cai *et al.* [54] are for large-area suspended graphene, where the two sets of data of Cai *et al.* correspond to different laser objectives used to heat the sample [20,54]. Three-dimensional units were obtained by dividing the conductivity Eq. (23) by the approximate thickness of a graphene sheet, 0.335 nm [10]. By including the work of Gu *et al.* [52] who studied the effects of four-phonon scattering on the thermal conductivity, we can consider the error associated

with only incorporating three-phonon scattering in our BTE formulation.

In Fig. 2, we first note that the present BTE-RTA slightly underestimates the conductivity relative to the three-phonon BTE results of Guo and Wang [10] and Gu *et al.* [52], around and below room temperature. As previously mentioned, an even larger underprediction has been noted in other studies [13–15,25]. With respect to the Callaway results of Guo and Wang, the relatively good agreement seen here may be due to our neglect of isotope scattering, which is present in their results, as well as our incorporation of optical phonons via the MD results of Zou *et al.* [24], which are not accounted for by Guo and Wang. The inclusion and exclusion of optical phonons and isotope scattering, respectively, serve to increase our conductivity relative to Guo and Wang, thereby partially offsetting the underprediction caused by our use of the RTA.

Our model agrees well with the four-phonon collision results of Gu *et al.* [52] at room temperature, but at higher temperatures tends towards the three-phonon collision results, as four-phonon collisions become more prevalent. The relatively good agreement between the present conductivity results and those obtained from the literature justifies the use of the parameters presented in Sec. II C.

B. Rescaling the BTE and MD

At temperatures much lower than the Debye temperature, direct comparisons between BTE and MD results are problematic because the classical equations of motion underlying MD do not capture quantum effects in the heat capacity. These effects are included in the BTE via the Bose-Einstein distribution, Eq. (6). However, by rescaling time and atomic mass in the BTE and MD equations, one can make the BTE correspond to a classical limit, where quantum effects are negligible. Such a rescaling allows for comparisons between both methods with a consistent heat capacity.

The classical equations of motion for a system of N particles are given by

$$\frac{d^2 x_i}{dt^2} = \frac{F_i(x_1, x_2, \dots, x_N)}{m_i}, \quad i = 1, 2, \dots, N, \quad (24)$$

where x_i , m_i , and F_i are the position, mass, and force acting on the i th particle, respectively. We rescale to a system of geometrically identical particles, but with masses increased by a scalar factor a^2 , i.e., $m_i \rightarrow a^2 m_i$. If time is then scaled by a factor a , or $t \rightarrow at$, the equations of motion Eq. (24) are unchanged.

We may perform a similar rescaling of the BTE to derive an equation free of quantum effects, analogous to MD. Consistent with our rescaling of time, we rescale frequency according to

$$\omega_l \rightarrow \frac{\omega_l}{a}. \quad (25)$$

With this frequency rescaling, the distribution function, g_{ω_l} , and the group velocity in Eq. (13) become

$$g_{\omega_l} \rightarrow a g_{\omega_l}, \quad (26)$$

and

$$v_{g,\omega_l} \rightarrow \frac{v_{g,\omega_l}}{a}, \quad (27)$$

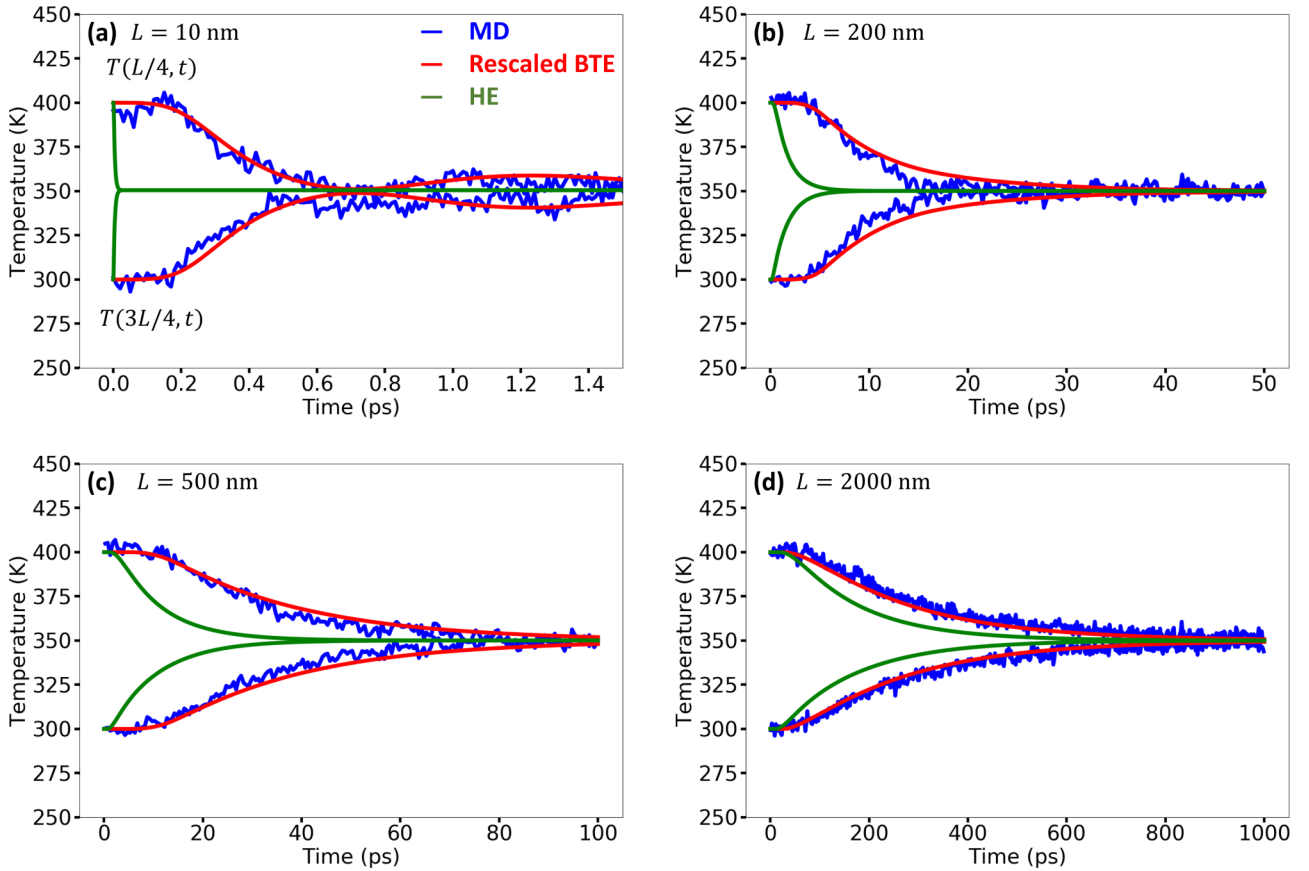


FIG. 6. (a) Transient temperatures $T(L/4, t)$ (top curves) and $T(3L/4, t)$ (bottom curves) with $T_0 = 350$ K for $L = 10$ nm, (b) $L = 200$ nm, (c) $L = 500$ nm, and (d) $L = 2000$ nm.

respectively. Rescaling time requires

$$\tau_{\omega_l} \rightarrow a\tau_{\omega_l}. \quad (28)$$

Substitution of Eqs. (25) to (28) and the time rescaling $t \rightarrow at$ into the BTE yields

$$\frac{\partial g_{\omega_l}}{\partial t} + \mathbf{v}_{g,\omega_l} \cdot \nabla g_{\omega_l} = \frac{1}{\pi} \frac{\tilde{C}_{\omega_l}|_{T_0} (T - T_0) - g_{\omega_l}}{\tau_{\omega_l}}, \quad (29)$$

where \tilde{C}_{ω_l} is the rescaled spectral heat capacity given by

$$\tilde{C}_{\omega_l} \Big|_{T_0} = \frac{(\hbar\omega_l)^2}{k_B(aT_0)^2} \frac{k}{2\pi v_{g,\omega_l}} \frac{e^{\hbar\omega_l/k_B(aT_0)}}{(e^{\hbar\omega_l/k_B(aT_0)} - 1)^2}, \quad (30)$$

and we used Eqs. (14) and (17). The rescaled BTE Eq. (29) is therefore unchanged, except for the term involving the heat capacity, where the factor a effectively increases the temperature, so that the heat capacity attains its constant, classical value. Equivalently, the factor a can be interpreted as reducing the Planck constant to zero, which has been done in other studies to derive a classical-based BTE [52].

In the limit that a becomes large, or in other words as the particle masses increase, \tilde{C}_{ω_l} approaches the classical heat capacity that follows as a consequence of Eq. (24) in the MD simulations. For large a , the rescaled BTE, Eq. (29), is equivalent to its original form, provided the spectral heat capacity is replaced by its constant, high temperature limit. Solution of the rescaled BTE permits direct comparisons

between the BTE and MD at a consistent heat capacity, with the understanding that we are now considering a pseudo-graphene system comprised of heavier atoms.

C. Nonlinear effects in C_ω

In Sec. II A, we assumed that the Bose-Einstein distribution f_{BE} varied linearly with temperature, leading to the linear form of the equilibrium distribution g_0 given by Eq. (4). Such a simplification yields what is known as the linearized Boltzmann transport equation [18], which is commonly used in studies involving three-phonon collisions [2]. Equation (4) is most accurate when T is close to T_0 , or when the heat capacity Eq. (5) does not change appreciably with temperature. Here, we test the limit of the linear approximation in graphene, as $T_{Hot} - T_{Cold}$ increases, and also examine the impact of including a quadratic term in Eq. (4). We verified that the third- and higher-order terms are negligible.

In Fig. 3, we plot transient temperature profiles for our graphene sheet, at the centers of the hot ($z = L/4$) and cold ($z = 3L/4$) regions, for the BTE both under the linear approximation, and including the second-order term in the expansion of f_{BE} . Figure 3(a) shows the results for $\Delta T_0 = 150$ K, where ΔT_0 is half the initial temperature difference, $\Delta T_0 = \frac{1}{2}(T_{Hot} - T_{Cold})$. We see that the BTE predicts an upward shift in the temperature profile when the second-order expansion is used, whereas the linear BTE misses this behavior. Similar, although less pronounced effects are observed in Fig. 3(b),

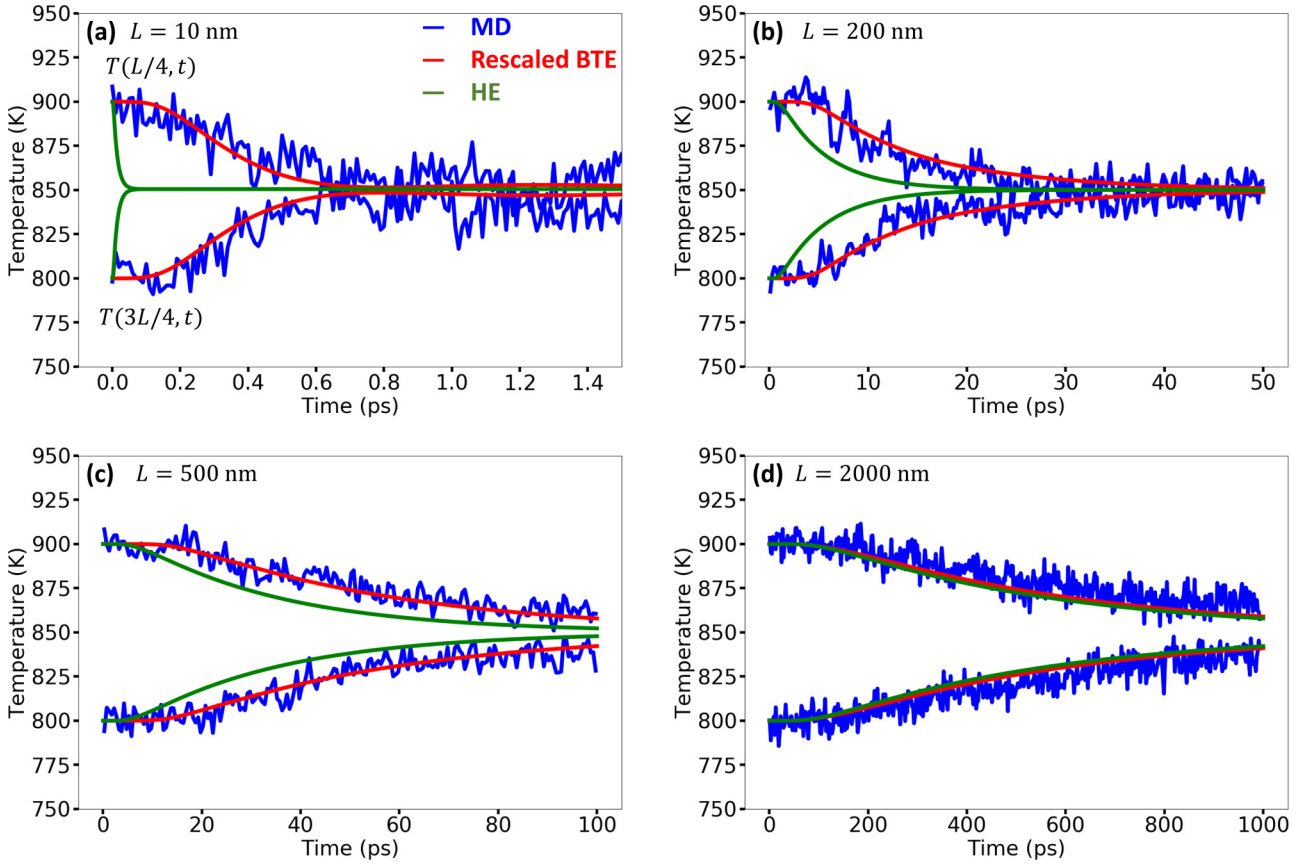


FIG. 7. (a) Transient temperatures $T(L/4, t)$ (top curves) and $T(3L/4, t)$ (bottom curves) with $T_0 = 850$ K for $L=10$ nm, (b) $L = 200$ nm, (c) $L=500$ nm, and (d) $L = 2000$ nm.

where $\Delta T_0 = 50$ K. We confirmed that the difference between the final temperature and the average of the initial temperatures for the second-order results in Figs. 3(a) and 3(b) are consistent with overall energy conservation. In the higher temperature simulations of Figs. 3(c) and 3(d), the linear and second-order BTE results are indistinguishable.

The upward shift observed in the colder simulations can be explained by the second-order expansion of f_{BE} introducing an effective temperature-dependent heat capacity. In the second-order case, the equilibrium distribution g_0 becomes

$$g_0 = \frac{1}{4\pi} C_{\omega_l} \Big|_{T_0} (T - T_0) + \frac{1}{4\pi} B_{\omega_l} \Big|_{T_0} (T - T_0)^2, \quad (31)$$

where

$$B_{\omega_l} \Big|_{T_0} = \frac{1}{2} \hbar \omega_l D_{\omega_l} \frac{\partial^2 f_{BE}}{\partial T^2} \Big|_{T_0}. \quad (32)$$

Now, defining

$$C_{\omega_l}^{(2)} = C_{\omega_l} \Big|_{T_0} + B_{\omega_l} \Big|_{T_0} (T - T_0), \quad (33)$$

allows us to write Eq. (31) as

$$g_0 = \frac{1}{4\pi} C_{\omega_l}^{(2)} (T - T_0). \quad (34)$$

Equation (34) is equivalent to Eq. (4), save for the temperature-dependent thermal conductivity $C_{\omega_l}^{(2)}$. The equivalence between the first- and second-order results of Figs. 3(c) and 3(d) is due to the heat capacity approaching its constant

limit at the elevated temperatures [B_{ω_l} in Eq. (33) goes to zero when evaluated at high temperatures], thus attenuating the temperature dependence in Eq. (34).

The nonlinear results presented here demonstrate that at around room temperature, ΔT_0 must be smaller than 50 K to justify the use of Eq. (4) in the BTE for graphene. However, since the BTE is unaffected by the inclusion of the second-order term in the high-temperature limit, the comparisons that follow, between the rescaled BTE (with classical heat capacity) and MD, are valid.

D. Comparison of BTE and MD predictions

We now compare transient results between the HE, rescaled BTE, and MD, for the temperature evolution in a graphene sheet, with initial condition shown in Fig. 1(b). We first consider a series of sheets of increasing length, ranging from 10 to 2000 nm, with $T_{Hot} = 600$ K, $T_{Cold} = 300$ K, $T_0 = 450$ K, and with the rescaled BTE heat capacity set to the constant high-temperature limit of $1.58 \times 10^{-3} \text{ J K}^{-1} \text{ m}^{-2}$. We verified that our results are numerically converged by independently varying the time step Δt , spatial step size Δz , number of frequency points N_ω , and number of angular points N_θ (see the Appendix).

Figures 4(a) to 4(d) shows the transient temperature profiles at the centers of the hot and cold regions, i.e., $z = L/4$ and $z = 3L/4$, respectively. We first note that the continuum model overpredicts the rates of heat transfer for all observed

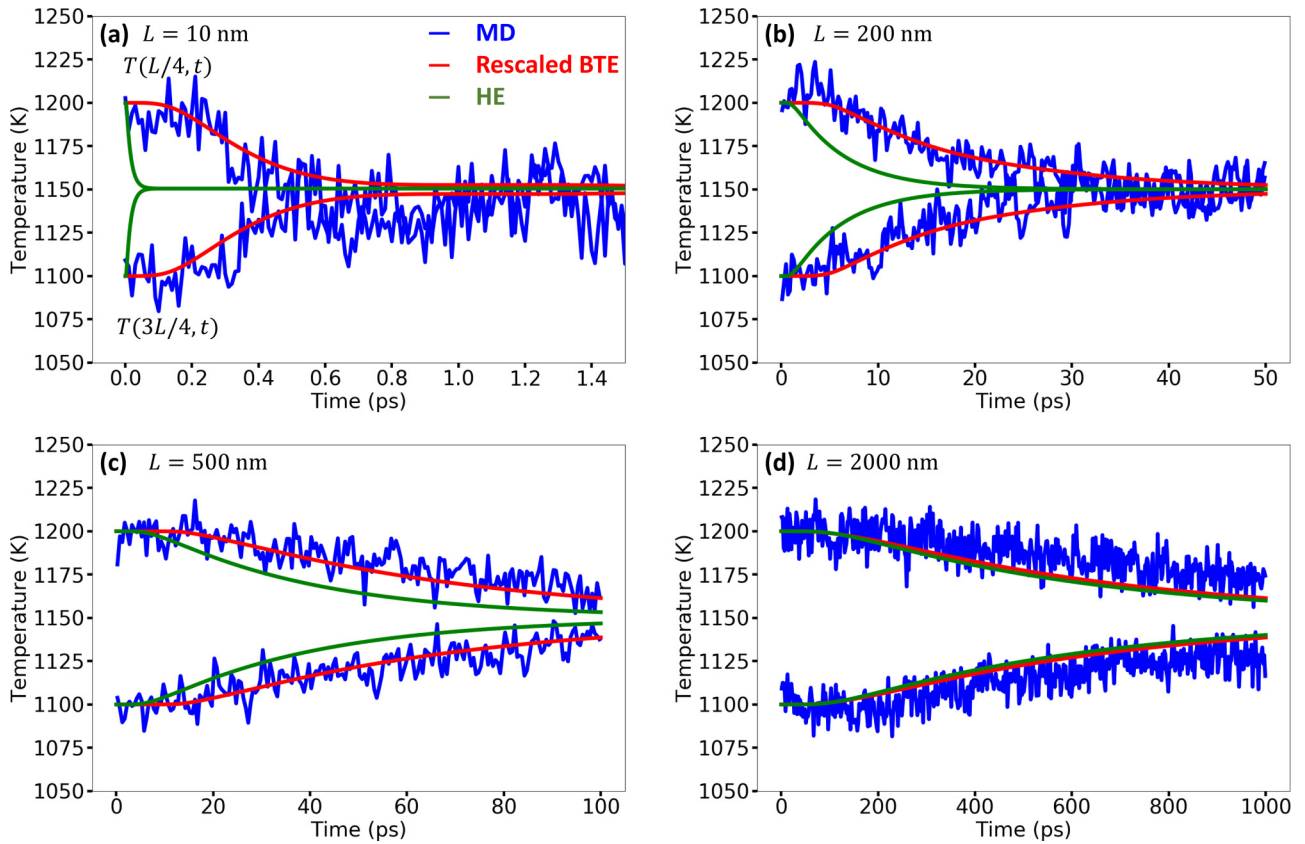


FIG. 8. (a) Transient temperatures $T(L/4, t)$ (top curves) and $T(3L/4, t)$ (bottom curves) with $T_0 = 1150$ K for $L = 10$ nm, (b) $L = 200$ nm, (c) $L = 500$ nm, (d) $L = 2000$ nm.

problem sizes, compared to the BTE and MD. The reason for this is that the parabolic form of the heat equation only accounts for the diffusion of heat, and does not capture ballistic transport. In contrast, the BTE and MD both predict ballistic phonon transport when length scales are small compared to the phonon mean free path. At room temperature, we calculated the weighted average mean free path (by the heat capacity) to be 260 nm, in agreement with other results [25]. As the problem size increases, the continuum results tend toward the BTE and MD predictions.

Generally good agreement is observed between the rescaled BTE and MD across all problem sizes, with maximum differences of $\sim 5\%$. There is better agreement for the smallest, 10-nm sheet, and the intermediate sized 500-nm sheet. Slightly underpredicted and overpredicted rates of heat transfer, relative to MD, are apparent for the 200- and 2000-nm sheets, respectively.

The excellent agreement for the 10-nm sheet is due to being in the ballistic regime, i.e., $\text{Kn} \gg 1$, so that the RTA scattering model is a minimal source of error in the BTE. To test the sensitivity to parameters in the RTA, we calculated results for 10- and 50-nm sheets, with relaxation times that were artificially increased to a level that rendered the collision term of the BTE negligible. The results are shown in Fig. 5, where they are labeled as “ballistic.” For the 10-nm case, we see that the ballistic and rescaled BTE results are almost identical, indicating that the 10-nm graphene sheet is in the nearly collision-free ballistic regime. However, in the larger, 50-nm sheet, the ballistic result deviates from the rescaled BTE result

because of the stronger effect of collisions at the lower Kn . Figure 5 confirms that, in the 10-nm results of Fig. 4(a), the excellent agreement between the rescaled BTE and MD is due to the insignificance of the RTA scattering term.

As the problem size in Fig. 4 increases above the ballistic limit, a ballistic-diffusive regime is entered where scattering becomes more prevalent. These effects are shown in Figs. 4(b) to 4(d), where lengths of 200, 500, and 2000 nm are considered. Due to our use of the RTA, slightly worse agreement is initially observed, where the rescaled BTE underpredicts the rate of heat transfer relative to MD, for the 200-nm sheet. The agreement then improves for the intermediate 500-nm sheet, and the rescaled BTE ultimately predicts slightly higher rates of heat transfer, relative to MD, for the largest, 2000-nm sheet.

A first possible explanation for the behavior in Figs. 4(b) to 4(d) is that upon entering the ballistic-diffusive regime, the assumption invoked by the RTA of being close to thermodynamic equilibrium is violated, i.e., the initial temperature difference between the hot and cold regions is too large to be considered a perturbation on an equilibrium state. To test this, we reduced T_{Hot} from 600 to 400 K, while keeping T_{Cold} at 300 K. Figures 6(a) to 6(d) shows the results for the reduced temperature simulations. Comparison with Figures 4(a) to 4(d) reveals qualitatively similar temperature profiles between the $\Delta T_0 = 50$ K and $\Delta T_0 = 150$ K cases. Therefore, the disagreements between the BTE and MD results in the ballistic-diffusive regime are unlikely to be due to large perturbations from equilibrium.

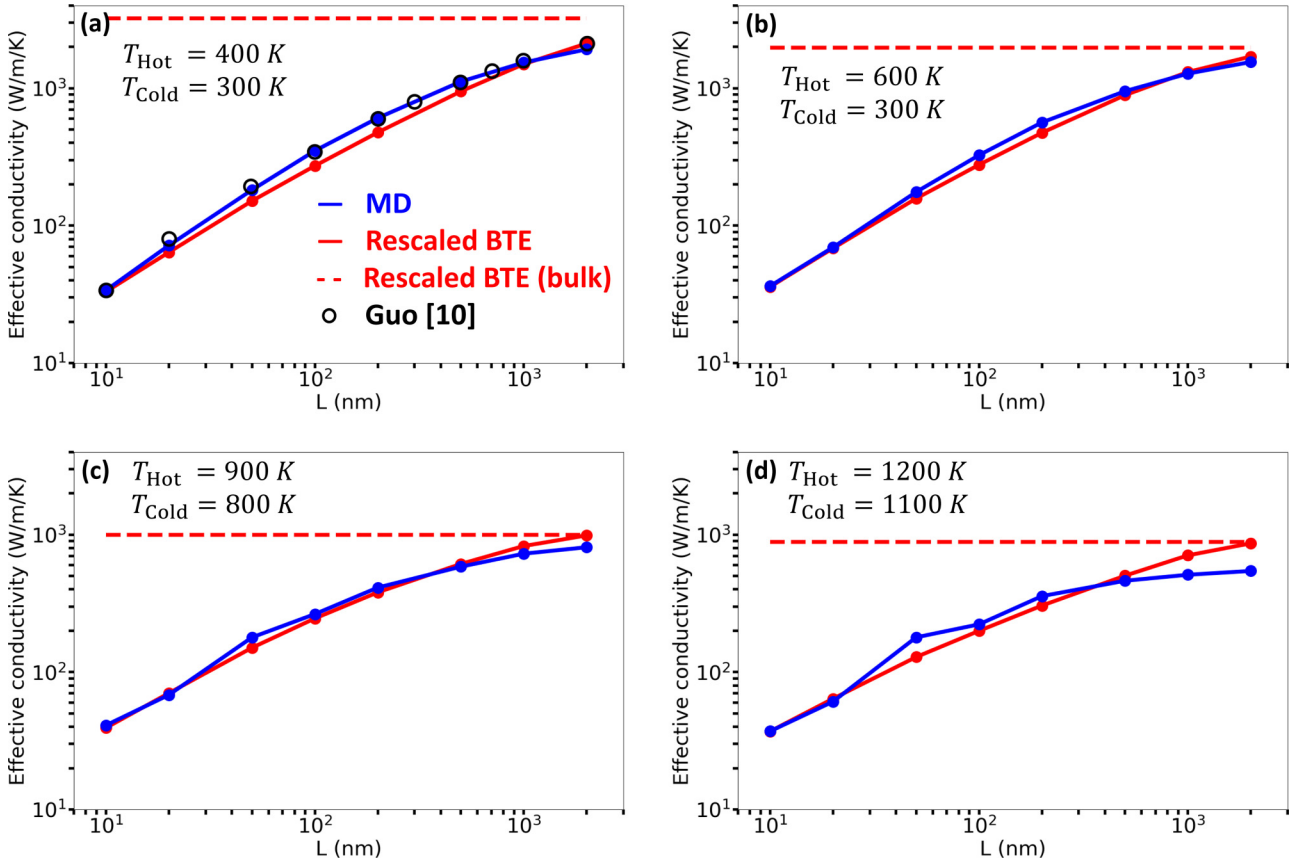


FIG. 9. Effective thermal conductivity as a function of problem size for (a) $T_0 = 350$ K, (b) $T_0 = 450$ K, (c) $T_0 = 850$ K, (d) $T_0 = 1150$ K. Results from Guo and Wang [10] are included.

Next, we test the performance of the BTE with the RTA at higher temperatures. Figures 7(a) to 7(d) and 8(a) to 8(d) show the results for the cases $T_{\text{Hot}} = 900$ K and $T_{\text{Hot}} = 1200$ K, respectively. Compared to the colder simulations, both sets of data show improved agreement between the rescaled BTE and MD, at $L = 200$ nm and $L = 500$ nm. Previous studies demonstrated that the BTE with the RTA underestimates the thermal conductivity in graphene, at room temperature, due to ignoring the collective effect of normal scattering [13–15,25]. As temperatures approach the Debye temperature of 2100 K [8], the relative importance of normal compared to Umklapp scattering diminishes [36], and the RTA should become more accurate. This may explain why the BTE-MD agreement improves for the $L = 200$ nm and $L = 500$ nm sheets, at the higher temperatures considered in Figs. 7 and 8.

As in the colder simulations, the rescaled BTE overpredicts the rate of heat transfer, relative to MD, for problem sizes approaching the continuum scale [Figs. 7(d) and 8(d)], where the rescaled BTE and HE results converge. The dominance of heat conduction in the continuum limit possibly magnifies the effect of neglecting four-phonon scattering in our BTE formulation, whose inclusion would lower the thermal conductivity in graphene [52,55].

To further quantify differences between the rescaled BTE and MD results, we calculated length-dependent effective thermal conductivities, by fitting both sets of data to the continuum heat equation, as described in Kroonblawd and Sewell [5]. Note that our fits included the complete time history over

the entire spatial domain, not just the $L/4$ and $3L/4$ points. Figures 9(a) to 9(d) shows the calculated effective conductivities for all four temperature differences that we considered, along with the bulk conductivities predicted by the rescaled BTE. For comparison, we also include in Fig. 9(a) values from Guo and Wang [10], who reported effective conductivities for a one-dimensional graphene sheet with isothermal boundaries, using the BTE with the Callaway collision model at 300 K.

As discussed previously, the best agreement between the rescaled BTE and MD results is observed for the smallest lengthscales, due to ballistic transfer being the dominant mode of heat transfer. We also see, as before, a trend for improved agreement between both methods in the intermediate ballistic-diffusive regime as temperatures increase. For the largest, 2000-nm sheets we considered, Figures 9(c) and 9(d) show effective conductivities that are 20% and 60% larger, respectively, compared to MD. In contrast, this overprediction is only 10% for the colder, $T_{\text{Hot}} = 400$ and 600 K sheets of Figs. 9(a) and 9(b). The increasing overestimation with temperature may be due to neglecting four-phonon scattering in our BTE formulation, the effects of which become more significant at higher temperatures [52,55], and when conduction is the dominant mode of heat transfer. Additionally, we see that in the continuum limit, the effective conductivities predicted by the rescaled BTE correctly converge towards the bulk values. Finally, we emphasize that the differences seen here in the rescaled BTE and MD effective conductivities

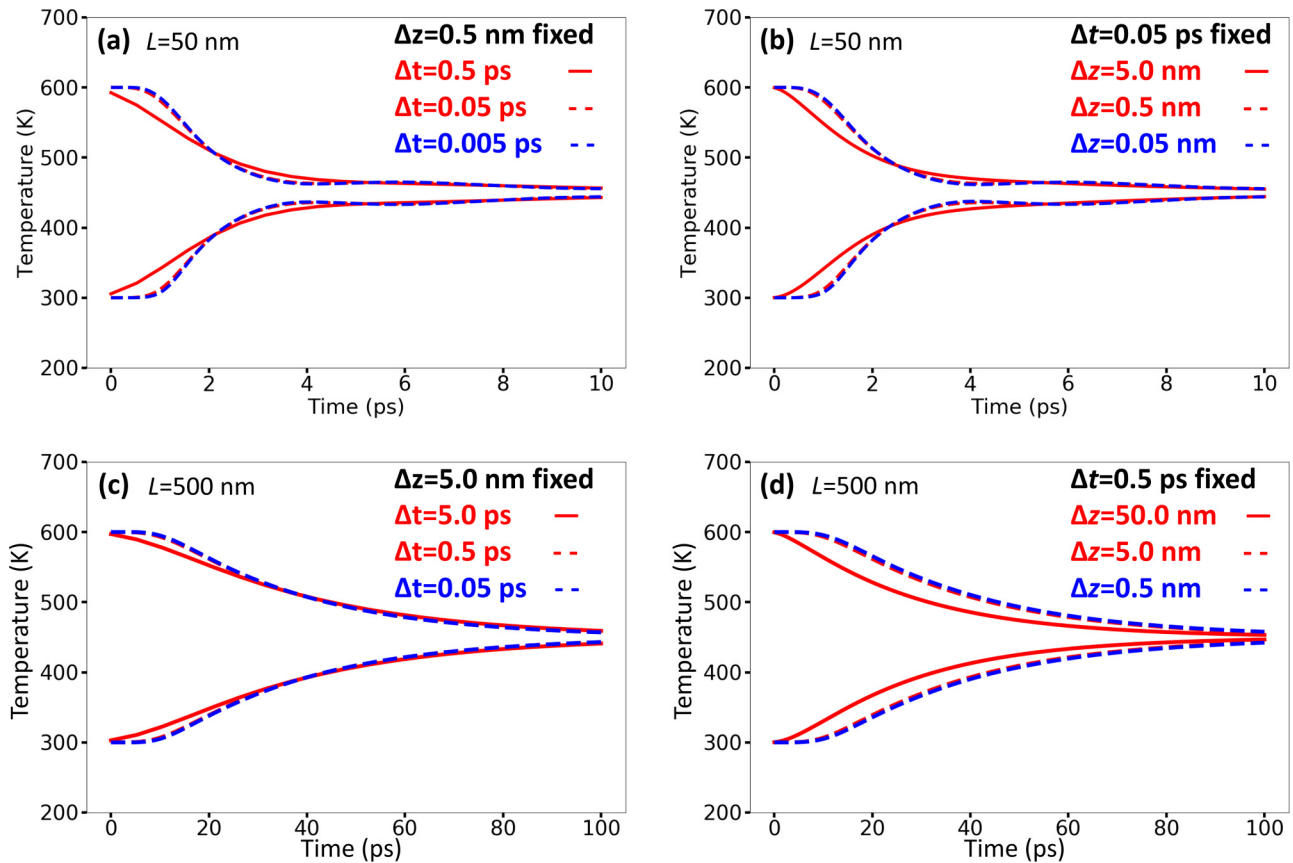


FIG. 10. Numerical convergence plots for (a) an $L = 50$ nm graphene sheet with $\Delta z = 0.5$ nm fixed, (b) $L = 50$ nm, $\Delta t = 0.05$ ps fixed, (c) $L = 500$ nm with $\Delta z = 5.0$ nm fixed, (d) $L = 500$ nm, $\Delta t = 0.5$ ps fixed.

only lead to maximum differences of $\sim 5\%$ in the transient temperature profiles.

V. CONCLUSION

In this work, we presented a framework for making accurate transient temperature predictions using the BTE with a simplified RTA scattering model. We calculated transient temperature profiles in graphene using the BTE, and developed a rescaling scheme to permit direct comparisons with analogous MD results in the classical limit. We demonstrated that the RTA is a computationally efficient alternative for transient thermal calculations in graphene, compared to MD, even for temperatures significantly below the Debye temperature. This method provides a means for studying transient heat transfer in situations inaccessible to approaches that include complete collision dynamics. Additionally, we demonstrated that the accuracy of our BTE formulation, relative to MD, is size- and temperature-dependent. The two methods yield nearly indistinguishable results in the ballistic limit, and when the effects of normal scattering are small. Our implementation depended on semi-empirical expressions for phonon scattering rates caused by Umklapp and normal scattering, as well as frequency-dependent parameters obtained from MD simulations. This work therefore demonstrates that, under many conditions of interest, the BTE can be an accurate and computationally efficient tool for exploring the physics of

nanoscale transient heat transfer if reliable phonon dispersion and relaxation-time parameters are available.

ACKNOWLEDGMENTS

This work was performed under the auspices of the U.S. Department of Energy by Lawrence Livermore National Laboratory under Contract DE-AC52-07NA27344.

APPENDIX: NUMERICAL CONVERGENCE

We tested for numerical convergence of our BTE results, with respect to the step sizes Δt and Δz , by varying each independently of each other. Results are shown in Fig. 10, for a graphene sheet with $L = 50$ nm, $T_{\text{Hot}} = 600$ K, and $T_{\text{Cold}} = 300$ K. In Fig. 10(a), we kept Δz fixed at 0.5 nm, and varied Δt . As in the main text, we plot the transient temperature profiles at the centers of the hot and cold regions, i.e., $z = L/4$ and $z = 3L/4$, respectively. We see that with respect to the time step, convergence is achieved when $\Delta t = 0.05$ ps. Similarly, in Fig. 10(b) we fixed $\Delta t = 0.05$ ps and varied Δz , and observed converged results when $\Delta z = 0.5$ nm. Therefore, in the simulation results presented in the main text for $L \geq 50$ nm, we set $\Delta t = 0.05$ ps and $\Delta z = 0.5$ nm. A similar procedure was performed for the 10-nm simulations, and we obtained converged results with $\Delta t = 0.01$ ps and $\Delta z = 0.1$ nm. We also varied N_ω and N_θ , and observed convergence for $N_\theta = 32$ and $N_\omega = 16$.

To verify that results for $L > 50$ nm with $\Delta t = 0.05$ ps and $\Delta z = 0.5$ nm are indeed converged, we carried out the previous procedure for an $L = 500$ nm sheet in Figs. 10(c) and 10(d). For the larger problem, convergence is achieved with a coarser mesh of $\Delta t = 0.5$ ps and $\Delta z = 5.0$ nm. However, as noted before, all results presented in the main text

where $L \geq 50$ nm were calculated with the finer mesh of $\Delta t = 0.05$ ps and $\Delta z = 0.5$ nm. Finally, we note that the convergence behavior shown in Fig. 10 was also checked and found to be unchanged at the higher temperature interval of 1200 K-1100 K, corresponding to Fig. 8 in the main text.

-
- [1] D. G. Cahill, W. K. Ford, K. E. Goodson, G. D. Mahan, A. Majumdar, H. J. Maris, R. Merlin, and S. R. Phillpot, Nanoscale thermal transport, *J. Appl. Phys.* **93**, 793 (2003).
- [2] A. J. Minnich, Advances in the measurement and computation of thermal phonon transport properties, *J. Phys.: Condens. Matter* **27**, 053202 (2015).
- [3] R. A. Austin, N. R. Barton, J. E. Reaugh, and L. E. Fried, Direct numerical simulation of shear localization and decomposition reactions in shock-loaded HMX crystal, *J. Appl. Phys.* **117**, 185902 (2015).
- [4] J. G. Christenson, R. A. Austin, and R. J. Phillips, Comparison of approximate solutions to the phonon Boltzmann transport equation with the relaxation time approximation: Spherical harmonics expansions and the discrete ordinates method, *J. Appl. Phys.* **123**, 174304 (2018).
- [5] M. P. Kroonblawd and T. D. Sewell, Anisotropic relaxation of idealized hot spots in crystalline 1,3,5-triamino-2,4,6-trinitrobenzene (TATB), *J. Phys. Chem. C* **120**, 17214 (2016).
- [6] G. Kumar, F. G. VanGessel, and P. W. Chung, Bond strain and rotation behaviors of anharmonic thermal carriers in α -RDX, *Propellants, Explosives, Pyrotechnics* **45**, 169 (2020).
- [7] J. M. Zaug, R. A. Austin, M. R. Armstrong, J. C. Crowhurst, N. Goldman, L. Ferranti, C. K. Saw, R. A. Swan, R. Gross, and L. E. Fried, Ultrafast dynamic response of single-crystal β -HMX (octahydro-1,3,5,7-tetranitro-1,3,5,7-tetrazocine), *J. Appl. Phys.* **123**, 205902 (2018).
- [8] E. Pop, V. Varshney, and A. K. Roy, Thermal properties of graphene: Fundamentals and applications, *MRS Bull.* **37**, 1273 (2012).
- [9] A. L. Moore and L. Shi, Emerging challenges and materials for thermal management of electronics, *Mater. Today* **17**, 163 (2014).
- [10] Y. Guo and M. Wang, Heat transport in two-dimensional materials by directly solving the phonon Boltzmann equation under Callaway's dual relaxation model, *Phys. Rev. B* **96**, 134312 (2017).
- [11] C. D. Landon and N. G. Hadjiconstantinou, Deviation simulation of phonon transport in graphene ribbons with *ab initio* scattering, *J. Appl. Phys.* **116**, 163502 (2014).
- [12] S. Lee, D. Broido, K. Esfarjani, and G. Chen, Hydrodynamic phonon transport in suspended graphene, *Nat. Commun.* **6**, 6290 (2015).
- [13] A. Cepellotti, G. Fugallo, L. Paulatto, M. Lazzeri, F. Mauri, and N. Marzari, Phonon hydrodynamics in two-dimensional materials, *Nat. Commun.* **6**, 6400 (2015).
- [14] G. Fugallo, A. Cepellotti, L. Paulatto, M. Lazzeri, N. Marzari, and F. Mauri, Thermal conductivity of graphene and graphite: Collective excitations and mean free paths, *Nano Lett.* **14**, 6109 (2014).
- [15] L. Lindsay, W. Li, J. Carrete, N. Mingo, D. A. Broido, and T. L. Reinecke, Phonon thermal transport in strained and unstrained graphene from first principles, *Phys. Rev. B* **89**, 155426 (2014).
- [16] A. Ward and D. A. Broido, Intrinsic phonon relaxation times from first-principles studies of the thermal conductivities of Si and Ge, *Phys. Rev. B* **81**, 085205 (2010).
- [17] X.-P. Luo, Y.-Y. Guo, M.-R. Wang, and H.-L. Yi, Direct simulation of second sound in graphene by solving the phonon Boltzmann equation via a multiscale scheme, *Phys. Rev. B* **100**, 155401 (2019).
- [18] G. Chen, *Nanoscale Energy Transport and Conversion: A Parallel Treatment of Electrons, Molecules, Phonons, and Photons* (Oxford University Press, New York, 2005).
- [19] Z. Aksamija and I. Knezevic, Lattice thermal conductivity of graphene nanoribbons: Anisotropy and edge roughness scattering, *Appl. Phys. Lett.* **98**, 141919 (2011).
- [20] Z. Aksamija and I. Knezevic, Lattice thermal transport in large-area polycrystalline graphene, *Phys. Rev. B* **90**, 035419 (2014).
- [21] Z. Aksamija and I. Knezevic, Thermal transport in graphene nanoribbons supported on SiO_2 , *Phys. Rev. B* **86**, 165426 (2012).
- [22] A. K. Majee and Z. Aksamija, Dynamical thermal conductivity of suspended graphene ribbons in the hydrodynamic regime, *Phys. Rev. B* **98**, 024303 (2018).
- [23] E. Pop, Energy dissipation and transport in nanoscale devices, *Nano Res.* **3**, 147 (2010).
- [24] J.-H. Zou, Z.-Q. Ye, and B.-Y. Cao, Phonon thermal properties of graphene from molecular dynamics using different potentials, *J. Chem. Phys.* **145**, 134705 (2016).
- [25] A. Cepellotti and N. Marzari, Thermal Transport in Crystals as a Kinetic Theory of Relaxons, *Phys. Rev. X* **6**, 041013 (2016).
- [26] S. G. Volz, Thermal Insulating Behavior in Crystals at High Frequencies, *Phys. Rev. Lett.* **87**, 074301 (2001).
- [27] *Microscale and Nanoscale Heat Transfer*, edited by S. Volz, (Springer-Verlag, Berlin, 2007).
- [28] J. Callaway, Model for lattice thermal conductivity at low temperatures, *Phys. Rev.* **113**, 1046 (1959).
- [29] B.-D. Nie and B.-Y. Cao, Thermal wave in phonon hydrodynamic regime by phonon Monte Carlo simulations, *Nanoscale Microscale Thermophys. Eng.* **24**, 94 (2020).
- [30] C. Hua and A. J. Minnich, Analytical Green's function of the multidimensional frequency-dependent phonon Boltzmann equation, *Phys. Rev. B* **90**, 214306 (2014).
- [31] M. Abramowitz and I. A. Stegun, *Handbook of Mathematical Functions: With Formulas, Graphs, and Mathematical Tables* (Dover, New York, 1972).
- [32] A. Stukowski, Visualization and analysis of atomistic simulation data with OVITO - the open visualization tool, *Model. Simul. Mater. Sci. Eng.* **18**, 015012 (2010), OVITO is available at <https://www.ovito.org>.

- [33] C. Zhang and Z. Guo, Discrete unified gas kinetic scheme for multiscale heat transfer with arbitrary temperature difference, *Int. J. Heat Mass Transf.* **134**, 1127 (2019).
- [34] E. N. Koukaras, G. Kalosakas, C. Galiotis, and K. Papagelis, Phonon properties of graphene derived from molecular dynamics simulations, *Sci. Rep.* **5**, 12923 (2015).
- [35] T. S. Fisher, *Thermal Energy at the Nanoscale* (World Scientific, Singapore, 2013).
- [36] A. A. Maznev and O. B. Wright, Demystifying umklapp vs normal scattering in lattice thermal conductivity, *Am. J. Phys.* **82**, 1062 (2014).
- [37] S. Mei, L. N. Maurer, Z. Aksamija, and I. Knezevic, Full-dispersion Monte Carlo simulation of phonon transport in micron-sized graphene nanoribbons, *J. Appl. Phys.* **116**, 164307 (2014).
- [38] A. K. Majee and Z. Aksamija, Length divergence of the lattice thermal conductivity in suspended graphene nanoribbons, *Phys. Rev. B* **93**, 235423 (2016).
- [39] D. T. Morelli, J. P. Heremans, and G. A. Slack, Estimation of the isotope effect on the lattice thermal conductivity of group iv and group iii-v semiconductors, *Phys. Rev. B* **66**, 195304 (2002).
- [40] B. D. Kong, S. Paul, M. B. Nardelli, and K. W. Kim, First-principles analysis of lattice thermal conductivity in monolayer and bilayer graphene, *Phys. Rev. B* **80**, 033406 (2009).
- [41] G. A. Slack and S. Galginaitis, Thermal conductivity and phonon scattering by magnetic impurities in CdTe, *Phys. Rev.* **133**, A253 (1964).
- [42] C. Herring, Role of low-energy phonons in thermal conduction, *Phys. Rev.* **95**, 954 (1954).
- [43] S. Plimpton, Fast parallel algorithms for short-range molecular dynamics, *J. Comput. Phys.* **117**, 1 (1995), LAMMPS is available at <http://lammps.sandia.gov>.
- [44] J. Tersoff, New empirical approach for the structure and energy of covalent systems, *Phys. Rev. B* **37**, 6991 (1988).
- [45] J. Tersoff, Modeling solid-state chemistry: Interatomic potentials for multicomponent systems, *Phys. Rev. B* **39**, 5566 (1989).
- [46] L. Lindsay and D. A. Broido, Optimized Tersoff and Brenner empirical potential parameters for lattice dynamics and phonon thermal transport in carbon nanotubes and graphene, *Phys. Rev. B* **81**, 205441 (2010).
- [47] S. Nosé, A unified formulation of the constant temperature molecular dynamics methods, *J. Chem. Phys.* **81**, 511 (1984).
- [48] W. G. Hoover, Canonical dynamics: Equilibrium phase-space distributions, *Phys. Rev. A* **31**, 1695 (1985).
- [49] G. J. Martyna, D. J. Tobias, and M. L. Klein, Constant pressure molecular dynamics algorithms, *J. Chem. Phys.* **101**, 4177 (1994).
- [50] M. P. Kroonblawd, N. Mathew, S. Jiang, and T. D. Sewell, A generalized crystal-cutting method for modeling arbitrarily oriented crystals in 3d periodic simulation cells with applications to crystal-crystal interfaces, *Comput. Phys. Commun.* **207**, 232 (2016).
- [51] See Supplemental Material at <http://link.aps.org/supplemental/10.1103/PhysRevB.102.205406> for code verification.
- [52] X. Gu, Z. Fan, H. Bao, and C. Y. Zhao, Revisiting phonon-phonon scattering in single-layer graphene, *Phys. Rev. B* **100**, 064306 (2019).
- [53] S. Chen, Q. Wu, C. Mishra, J. Kang, H. Zhang, K. Cho, W. Cai, A. A. Balandin, and R. S. Ruoff, Thermal conductivity of isotopically modified graphene, *Nat. Mater.* **11**, 203 (2012).
- [54] W. Cai, A. L. Moore, Y. Zhu, X. Li, S. Chen, L. Shi, and R. S. Ruoff, Thermal transport in suspended and supported monolayer graphene grown by chemical vapor deposition, *Nano Lett.* **10**, 1645 (2010).
- [55] T. Feng and X. Ruan, Four-phonon scattering reduces intrinsic thermal conductivity of graphene and the contributions from flexural phonons, *Phys. Rev. B* **97**, 045202 (2018).